ELLAS

Enhancing LiDAR Perception With Location-Aware Scanning Profile Adaptation

Rhemrev, Thymon; De Jong, Emma; Van Triest, Gideon; Kalkman, Roger; Pronk, Jordy; Pandharipande, Ashish; Jonathan Myers, Nitin

DOI
10.1109/JSEN.2025.3526733

Publication date
2025

Document Version
Final published version

Published in
IEEE Sensors Journal

ELLAS: Enhancing LiDAR Perception With Location-Aware Scanning Profile Adaptation

Thymon Rhemrev, Emma de Jong, Gideon van Triest, Roger Kalkman, Jordy Pronk, Ashish Pandharipande, *Senior Member, IEEE*, and Nitin Jonathan Myers, *Member, IEEE*

***Abstract*—Light detection and ranging (LiDAR) is used in robots and in automotives to obtain the perception of the surrounding environment. Traditional spinning LiDARs scan the environment uniformly along all angular directions by operating at a constant rotational speed, with fixed sensing parameters throughout a rotation. Such a sensing approach, however, is suboptimal when information about static obstacles in the environment is available at the LiDAR. In this work, we introduce ELLAS, a first-of-its-kind spinning LiDAR system that dynamically adapts its range and resolution over the field of view. This adaptation is achieved by optimizing the ranging parameters at the LiDAR and the instantaneous rotational speed of the spinning platform to the location of static objects in scene topology maps. With the optimized settings, ELLAS results in a longer range along directions where static obstacles are farther away and achieves a higher angular resolution around those directions.**

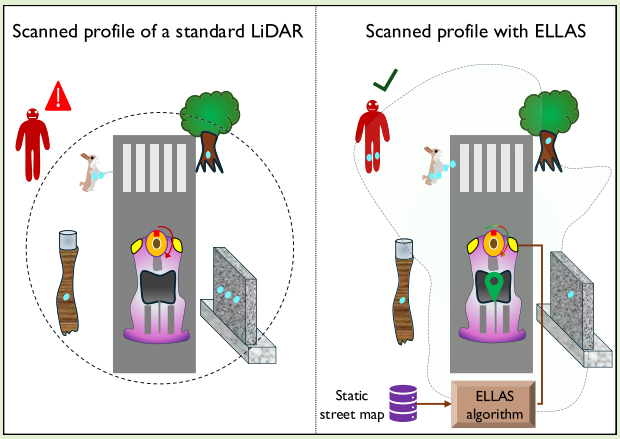

***Index Terms*— Automotive, directional range adaptation, resolution adaptation, situation-aware sensing, spinning light detection and ranging (LiDAR).**

I. Introduction

THERE is a growing interest in deploying autonomous vehicles for both indoor industrial applications and outdoor driving [1], [2], [3]. These vehicles must perceive their surroundings to navigate through complex environments. Light detection and ranging (LiDAR) is an important sensing modality employed in autonomous vehicles to achieve this perception. Current-generation commercial LiDARs have a higher angular resolution than radars [4], [5], which allows them to distinguish between two closely spaced targets.

Spinning LiDAR systems are used in navigation robots and automotives [3], [6], [7], [8] to scan the environment. These systems mount a pencil beam LiDAR on a mechanically rotating platform. At any given time instant, the LiDAR directs its power along a specific direction by transmitting a light signal. This signal reflects off a target, and the reflected signal is captured by the LiDAR receiver. By analyzing the reflected signal, the system calculates the range of the target in the scanned direction. The spinning mechanism in these systems enables a 360° perception of the environment, with the spin rate varying by application. For instance, the automotive spinning LiDAR in [8] rotates at about 600 r/min, equivalently 10 frames per second (fps).

Existing spinning LiDAR systems operate at a constant rotational speed and use the same sensing parameters throughout a rotation. As a result, the maximum range up to which the LiDAR can detect is constant across all directions. Such a constant scanning range profile is suboptimal under location awareness in the form of scene topology maps [9], [10]. These maps can provide coordinates of several static obstacles, such as guard rails, lamp-posts, and buildings, around the automotive. In an indoor setup, such static scene topology maps can be derived from floor plans with information on furniture and walls. A LiDAR can make use of this information

Received 20 November 2024; revised 31 December 2024; accepted 2 January 2025. Date of publication 15 January 2025; date of current version 28 February 2025. This work was supported in part by the High Tech Visibility Boost Grant from the Faculty of Mechanical Engineering, Delft University of Technology, The Netherlands; in part by NXP Semiconductors Inc.; and in part by Netherlands Enterprise Agency under Grant PPS2207. An earlier version of this paper was presented at the IEEE Sensors 2024 Conference. The associate editor coordinating the review of this article and approving it for publication was Dr. Muhammad Ali Jamshed. *(Corresponding author: Nitin Jonathan Myers.)*

Thymon Rhemrev, Emma de Jong, Gideon van Triest, Roger Kalkman, and Jordy Pronk are with Delft Center for Systems and Control, Delft University of Technology, 2628 CD Delft, The Netherlands.

Ashish Pandharipande is with NXP Semiconductors, 6534 AE Nijmegen, The Netherlands (e-mail: ashish.pandharipande@nxp.com).

Nitin Jonathan Myers is with Delft Center for Systems and Control, Delft University of Technology, 2628 CD Delft, The Netherlands (e-mail: N.J.Myers@tudelft.nl).

A live demonstration of this work is available online at https://www.youtube.com/watch?v=DYse8EQgHYI.

Digital Object Identifier 10.1109/JSEN.2025.3526733

to adapt its scanning technique to the scene. For example, if a static obstacle is known to be 1 m away in a specific direction, the LiDAR need not allocate its resources to scan the occluded region beyond that distance. Such direction-dependent range adaptation conserves time and allows for more efficient detection in other directions. To the best of our knowledge, ELLAS is the first system to use location-based static scene topology maps, such as offline street maps, to adapt LiDAR sensing.

Previous research on adaptive LiDAR systems has mainly focused on foveation, a process that enhances the density of point cloud samples in regions of interest (RoIs). Missing depth information in the field of view (FoV) is subsequently estimated using inpainting techniques. For example, the RoI in [11] included moving targets, with their boundaries determined from a co-located camera. In [12] and [13], the LiDAR scan was adapted over multiple iterations to image the FoV, with the sampling coordinates optimized in each iteration to enhance the information inferred from previous iterations. Finally, Tilmon et al. [14] proposed adaptive sampling as well as optical power control over the FoV for depth estimation in wearable devices, thereby enabling joint range and resolution adaptation while considering eye safety aspects.

In contrast to past works, our paper focuses on maximizing the scanned envelope of a spinning LiDAR under system-level constraints and scene awareness. In ELLAS, the FoV is partitioned into several sectors in the angle domain. The scanned range and the angular resolution in the sectors are both optimized to the static environment around the LiDAR, to enhance detection within the unoccluded region. The contributions in this article are listed below.

1) We design an adaptive spinning platform in ELLAS that can seamlessly integrate with most programmable off-the-shelf LiDARs. Our platform can simultaneously adjust both the instantaneous spin rate and the ranging parameters of the LiDAR over different sectors.
2) We formulate a convex optimization program to jointly optimize the spin rate and the ranging parameters at the LiDAR over a rotation. Our problem incorporates static scene topology map information at the LiDAR's location. Furthermore, it also accounts for the mechanical constraints on the spinning platform and the optical characteristics of the LiDAR sensor.
3) We build an end-to-end indoor navigation system to demonstrate ELLAS. In our setup, the navigating robot wirelessly transmits its location to a local server. The server, using a predetermined static map of the environment, solves the proposed optimization problem. Finally, the optimized spin rates and ranging parameters are sent back to the LiDAR, which acquires a point cloud and relays it to the server for visualization.

To demonstrate ELLAS, we use the VL53L1X time-of-flight (ToF) LiDAR sensor that has a maximum range of 4 m [15]. While our prototype can achieve a frame rate of up to 0.65 fps, due to the mechanical constraints on the maximum spin rate, the ELLAS design can, however, scale to automotive LiDAR systems that feature a higher spin rate and a longer detection range.

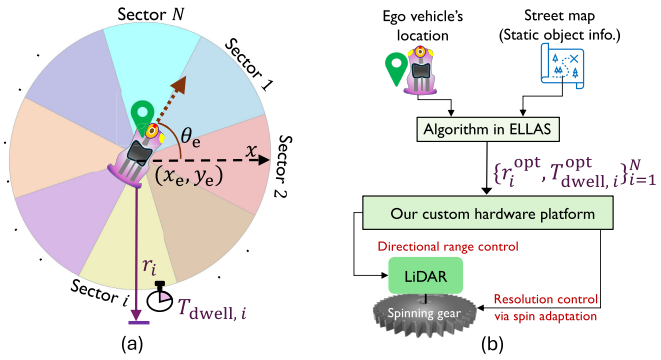

Fig. 1. In this work, the LiDAR's 360° FoV is partitioned into N equal sectors. In sector i, the dwell time $T_{\text{dwell},i}$ is the time spent by the LiDAR and r_i is its scanned range. ELLAS optimizes both r_i and $T_{\text{dwell},i}$ over all the N sectors using location-based static scene topology maps. (a) Sectors in LiDAR's FoV. (b) System in ELLAS.

ELLAS differs from our recent work on scene-aware automotive radar sensing [16], [17], [18] in the following aspects. First, [16], [17], [18] consider an automotive phased-array radar in comparison to a spinning LiDAR in this work. As such, in our past works, we optimized the scanned range over different directions through adaptive beamforming, while ELLAS optimizes the angular resolution in addition to the range. Second, ELLAS allocates time resources over a rotation based on scene awareness, whereas [16], [17], [18] focuses on power resource allocation. Finally, ELLAS implements an end-to-end system for scene-aware LiDAR sensing.

II. System Model for Adaptive Spinning LiDARs

A spinning LiDAR system consists of a LiDAR unit mounted on a rotating platform. By dynamically adapting the spin rate and sensing parameters over a rotation, the LiDAR's scanning range and resolution over the FoV can be tuned in real time. ELLAS leverages static scene topology maps to perform this adaptation over different sectors in the FoV. The sectors are illustrated in Fig. 1(a) and a schematic of the proposed system is shown in Fig. 1(b). In this section, we discuss constraints in a spinning LiDAR which will be incorporated in our optimization problem. We also sketch the feasible region corresponding to some constraints, for our hardware implementation.

A. Dwell Time Constraint Due to the Spinning Platform

Consider an ego vehicle at the location (x_e, y_e) heading at an angle of θ_e with respect to the x-axis. The 360° FoV around the ego vehicle is partitioned into N distinct sectors starting from the heading direction, as shown in Fig. 1. In this article, we consider sectors of equal angular width of $2\pi/N$. We define $\mathcal{S}_i$ as the set consisting of scanning directions, measured with the positive x-axis, in sector i. Then

$$\mathcal{S}_i = \{\theta : \theta_e - 2\pi(i-1)/N \leq \theta < \theta_e - 2\pi i/N\}. \quad (1)$$

We define T as the time period of the spinning LiDAR. As the LiDAR spins on the rotating platform, it spends a fraction of this total time period in scanning a sector. The frame rate corresponding to T is defined as $F = 1/T$. We define the

dwell time $T_{\text{dwell},i}$ as the time spent by the LiDAR in scanning the ith sector. Therefore

$$\sum_{i=1}^{N} T_{\text{dwell},i} = T = \frac{1}{F}. \tag{2}$$

The mechanical constraints on the rotor impose a maximum rotational speed limit denoted by $\omega_{\max}$. Under this constraint, the dwell time $T_{\text{dwell},i}$ is lower bounded by the following equation:

$$T_{\text{dwell},i} \geq \frac{2\pi/N}{\omega_{\max}}. \tag{3}$$

By leveraging scene awareness, ELLAS optimizes the dwell time in each sector under several constraints including those in (2) and (3).

B. Ranging Duration Limits at the LiDAR Sensor

We now explain the signaling mechanism of our LiDAR and introduce the ranging duration needed to reliably scan a specified distance. A typical LiDAR transmits a time-domain waveform, such as a pulse, over a narrow beam into the environment. This waveform reflects off a target in the illuminated direction and is received after a delay proportional to the target's range. In a ToF LiDAR, the time difference between the transmitted and received pulses is calculated to determine the range. The maximum scanning range in a ToF system is governed by the time lapse between successive pulses emitted as well as the received signal-to-noise ratio (SNR).

We define the ranging duration $\delta(r)$ as the time spent by the LiDAR to reliably scan up to a maximum range of r. The minimum time needed to scan this distance is defined as $\delta_{\min}(r)$, that is, $\delta(r) \geq \delta_{\min}(r)$. To unambiguously scan a range up to r, a ToF LiDAR must space its pulse transmissions by at least $2r/c$ [19], where c is the speed of light. Thus, the scanning range desired in a sector places a lower bound on the time between successive transmissions,[1] that is, $\delta_{\min}(r) \geq 2r/c$. To ensure sufficient SNR for reliable detection, a LiDAR may transmit multiple pulses in a given interval. The number of pulses needed depends on the ambient lighting level (noise level), with stronger ambient light requiring an increased pulse count to reliably measure distance. Under such conditions, $\delta(r)$ must be substantially larger than $2r/c$.

Constraint in Our Setup: In this article, we use the VL53L1X sensor [15] and find $\delta(r)$ as a function of r experimentally, for an ambient lighting level of 295 lx (lumens per square meter). In this experiment, we place a target at a distance of r from the LiDAR. Then, the LiDAR's ranging duration, which determines the number of emitted pulses, is progressively decreased until the measured distance has an error of at least 1 cm. The resultant ranging duration is defined as $\delta_{\min}(r)$ and depicted in Fig. 2.

[1]The minimum ranging duration is directly related to the maximum refresh rate of a LiDAR. Specifically, the maximum refresh rate associated with $\delta_{\min}(r)$ is $1/\delta_{\min}(r)$.

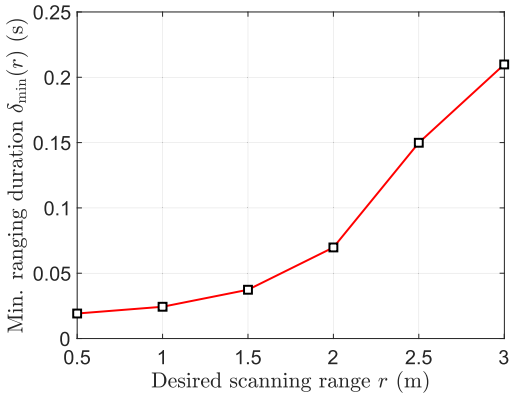

Fig. 2. Minimum ranging duration $\delta_{\min}(r)$ needed to reliably scan up to a distance r with the VL-53L1X LiDAR. Here, the ambient lighting level was 295 lx. We set short-, medium-, and long-distance modes at the LiDAR when scanning the distance ranges [0, 1.5 m), [1.5, 3 m), and [3, 4 m).

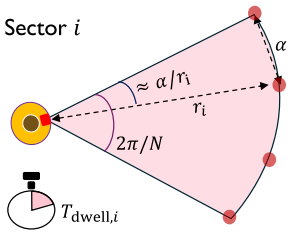

Fig. 3. Angular resolution needed to achieve a spatial resolution of α at r_i is about α/r_i. The resolution requirement imposes a bound on the dwell time $T_{\text{dwell},i}$, as derived in (6).

C. Dwell Time Constraint for a Desired Spatial Resolution

We derive constraints on the dwell time to achieve a desired spatial resolution of α. For the ith sector, we show that this constraint also depends on the desired scanned range r_i. We consider the ith sector in which the LiDAR spends $T_{\text{dwell},i}$ amount of time (see Fig. 3). To achieve a spatial resolution of α at the desired scanned range r_i, the LiDAR must scan the sector with an angular resolution of

$$\Delta_{\theta,i} = 2\sin^{-1}\left(\frac{\alpha}{2r_i}\right) \approx \alpha/r_i. \tag{4}$$

The approximation in (4) is valid as $\alpha \ll r_i$ in typical LiDAR applications. Note that $\Delta_{\theta,i}$ in (4) achieves higher spatial resolution than α at distances smaller than r_i. We translate the resolution requirement in (4) into a requirement on the point cloud density. As the central angle of any sector is $2\pi/N$, the LiDAR should be capable of acquiring

$$P_i = \left\lceil \frac{2\pi/N}{\Delta_{\theta,i}} \right\rceil \tag{5}$$

point cloud measurements at the desired scanned range r_i. Here, $\lceil\cdot\rceil$ is the ceil operator. As the LiDAR must spend at least $\delta_{\min}(r_i)$ time to acquire one measurement at r_i, it follows that the dwell time $T_{\text{dwell},i}$ must be no smaller than $P_i\delta_{\min}(r_i)$. Using (4) and (5), we can write this constraint as follows:

$$T_{\text{dwell},i} \geq \left\lceil \frac{2\pi r_i}{N\alpha} \right\rceil \delta_{\min}(r_i) \quad \forall i \in [N] \tag{6}$$

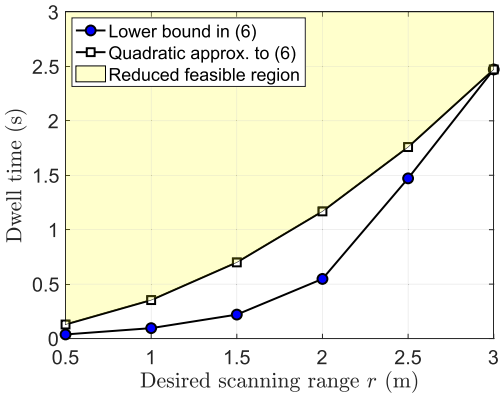

Fig. 4. To reliably scan up to a distance of r in a sector, the LiDAR's dwell time in that sector needs to be at least the lower bound in (6). The lower bound for our setup is shown here for $N = 8$ and $\alpha = 20$ cm. The reduced feasible region comprises all range-dwell time combinations over our quadratic approximation of (6).

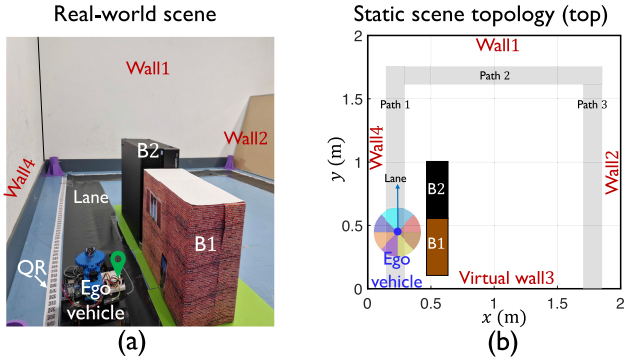

Fig. 5. Miniature driving scenario and the top view of its corresponding static scene topology map. Here, the map comprises two buildings (B1, B2) and four walls. ELLAS leverages this map to optimize the LiDAR's scanning profile. (a) Real-word scene. (b) Static scene topology (top).

where $[N]$ denotes the set $\{1, 2, 3, \ldots, N\}$. We observe from (6) that a longer dwell time is needed to scan farther distances.

We now motivate the quadratic approximation to the bound in (6). ELLAS optimizes the pair $(r_i, T_{\text{dwell},i})$ over all the N sectors, while ensuring that the constraint in (6) is satisfied for all $i \in [N]$. To this end, we find a quadratic upper bound on $\lceil 2\pi r_i/(N\alpha)\rceil \delta_{\min}(r)$ and construct a reduced feasible region, which is a subset of the region associated with (6). A sketch of this region is shown in Fig. 4 for our setup. A quadratic upper bound, which forms the boundary of the reduced feasible region, is chosen for two reasons. First, a quadratic constraint represents a convex set, which is easier to encode in our solver compared to (6). Second, the upper bound provides a safety margin on the dwell time, ensuring that the optimized solution remains feasible even at a slightly higher ambient lighting level.

To derive the quadratic upper bound, we use the scanned range and the minimum dwell time combinations obtained from our experiment. A total of K combinations, each represented as $(r^k, T^k_{\text{dwell}})$, are obtained, where k indicates the index of each data point. We define the quadratic upper bound on $\lceil 2\pi r_i/(N\alpha)\rceil \delta_{\min}(r)$ as $\beta_2 r^2 + \beta_1 r + \beta_0$, where β_2, β_1, and β_0 are parameters to be estimated. These parameters are found by solving

$$(\beta_2^\star, \beta_1^\star, \beta_0^\star) = \operatorname{argmin} \beta_2^2 + \beta_1^2 + \beta_0^2$$
$$\text{s.t. } \beta_2 (r^k)^2 + \beta_1 r^k + \beta_0 \geq T^{(k)}_{\text{dwell}} \quad \forall k \in [K]. \tag{7}$$

The problem in (7) minimizes the ℓ_2 norm of the parameter vector $(\beta_2, \beta_1, \beta_0)$ subject to linear constraints. The reduced feasible region, defined by the quadratic bound, can then be expressed as follows:

$$T_{\text{dwell},i} \geq \beta_2^\star r_i^2 + \beta_1^\star r_i + \beta_0^\star \quad \forall i \in [N]. \tag{8}$$

Constraint in Our Setup: To find the reduced feasible region, we first compute the lower bound in (6) using $K = 6$ scanned range and minimum dwell time combinations obtained from our experiment. These six combinations, marked as blue circles in Fig. 4, are found by using (6) over the datapoints in Fig. 2. For our setup, the lower bound is sketched in Fig. 4 for $N = 8$ sectors and $\alpha = 20$ cm. Next, the six scanned range and minimum dwell time combinations are encoded as six linear constraints in (7). For the measured data points in our experiment, the solution to (7) was $(\beta_2^\star, \beta_1^\star, \beta_0^\star) = (0.26, 0.08, 0.03)$. The corresponding dwell time constraint for sector i is then $T_{\text{dwell},i} \geq 0.26\, r_i^2 + 0.08\, r_i + 0.03$. This constraint, which represents the reduced feasible region, is shown in Fig. 4.

III. Scene-Aware LiDAR Sensing in ELLAS

In this section, we explain how to derive scene awareness of the ego vehicle from static scene topology maps. We then incorporate scene awareness as a constraint in our optimization problem to adapt the LiDAR scan. To aid our explanation, we use the setup shown in Fig. 5(a). While we use Fig. 5(a) as an illustrative example, our procedure to derive scene awareness and our optimization formulation generalizes to any arbitrary scenario.

Our setup in Fig. 5(a) is a miniature driving scenario in a 2×2 m floor space. It features two small buildings centered at $(55, 33$ cm) and $(55, 78$ cm). The buildings are next to each other and they have the same dimensions $(x \times y \times z)$ of $17 \times 45 \times 60$ cm. Fig. 5(b) shows the static scene topology map corresponding to our setup in Fig. 5(a). The static scene topology map at the ego vehicle comprises a digital model of all known static obstacles, such as buildings (B1 and B2) and the four walls within the environment. In this article, we use a binary occupancy grid map as a static scene topology map. This map is 1 at the static obstacle locations and is 0 otherwise. Our ego vehicle is a robot equipped with a spinning LiDAR and is represented as a blue dot in Fig. 5(b). The robot navigates along the paths marked in Fig. 5(b).

ELLAS exploits scene awareness at the ego vehicle in the form of a digital representation of the static environment, an example of which is shown in Fig. 5(b). In real-world automotive driving applications, vehicles can access similar maps using services like Google Street Maps. The digital static map information can be leveraged to adapt how the ego vehicle's LiDAR scans the scene. Specifically, the LiDAR

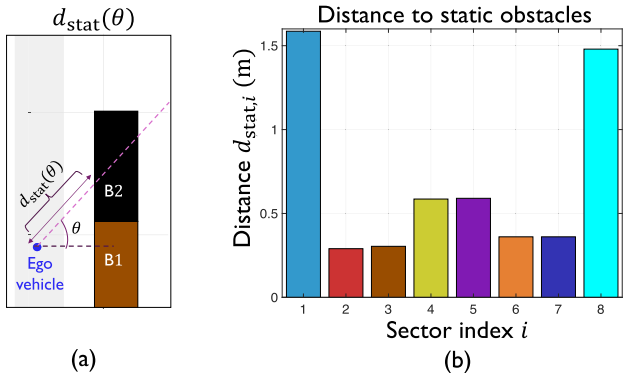

Fig. 6. Here, $d_{\text{stat}}(\theta)$ is the distance between the ego vehicle and the first known static obstacle along direction θ. The function $d_{\text{stat}}(\theta)$ is used to find $d_{\text{stat},i}$ in sector i using (9). Fig. 5(b) shows $d_{\text{stat},i}$s for $N = 8$ sectors. Here, $(x_e, y_e) = (0.24, 0.45\text{ m})$ and $\theta_e = 90°$. The colors in the bar graph correspond to those of the sectors marked in Fig. 5(b). (a) $d_{\text{stat}}(\theta)$. (b) Distance to static obstacles.

need not scan beyond the closest known static obstacle in any direction, as this obstacle occludes all targets that are farther away along that direction. Furthermore, the LiDAR can spin faster and reduce its angular resolution around directions with closer static obstacles. This allows the LiDAR more time to scan critical sectors such as those focusing along the lane.

Using the static scene topology map and the ego vehicle's pose (location and orientation), the distance to the first known static obstacle along any direction can be computed from geometry. We define $d_{\text{stat}}(\theta)$ as this distance along direction θ. An example illustrating $d_{\text{stat}}(\theta)$ is shown in Fig. 6(a) for the topology in Fig. 5(b). As ELLAS optimizes the LiDAR's parameters at the sector level, the maximum of all the $d_{\text{stat}}(\theta)$s in a sector is used for optimization. To this end, we construct

$$d_{\text{stat},i} = \max_{\theta \in \mathcal{S}_i} \; d_{\text{stat}}(\theta) \tag{9}$$

for each sector i. Note that $d_{\text{stat},i}$ changes with the ego vehicle's pose. For $(x_e, y_e) = (0.24, 0.45\text{ m})$ and $\theta_e = 90°$, we show $d_{\text{stat},i}$ in Fig. 6(b) for the topology in Fig. 5(b). We observe that this distance is smaller in sectors 2-7 that face the buildings (B1 and B2) or wall 4. The directionally invariant range profile with standard LiDARs is often suboptimal in environments with a nonuniform static distance profile, such as the one in Fig. 6(b).

A. Optimization Problem in ELLAS

ELLAS tailors the LiDAR's scanning profile to $\{d_{\text{stat},i}\}_{i=1}^N$, by jointly optimizing the scanned range r_i and the dwell time $T_{\text{dwell},i}$ over all the N sectors. The key idea in ELLAS is to enhance the scanned envelope under scene awareness and hardware constraints at the LiDAR. To this end, the sum of scanned ranges over all the sectors, that is, $\sum_{i=1}^N r_i$, is maximized as done in [17]. The maximization is performed under scene awareness and the dwell time constraints in (2), (3), and (8). In this article, we model scene awareness as a constraint that enforces that the LiDAR's scanned range r_i does not exceed $d_{\text{stat},i}$, that is,

$$r_i \le d_{\text{stat},i} \quad \forall i \in [N]. \tag{10}$$

We put these observations together to formulate our optimization problem

$$\begin{aligned} \max_{\{r_i\}_1^N, \{T_{\text{dwell},i}\}_1^N} \; & \sum_{i=1}^N r_i \\ \text{s.t. } & r_i \le d_{\text{stat},i} \quad \forall i \in [N] \\ & T_{\text{dwell},i} \ge \frac{2\pi/N}{\omega_{\max}} \quad \forall i \in [N] \\ & \sum_{i=1}^N T_{\text{dwell},i} = \frac{1}{F} \\ & T_{\text{dwell},i} \ge \beta_2^\star r_i^2 + \beta_1^\star r_i + \beta_0^\star \quad \forall i \in [N]. \end{aligned} \tag{11}$$

The problem in (11) jointly optimizes the range and the resolution of the LiDAR over different sectors, unlike the method in [17] which only adapts the range of radar over the sectors and ignores resolution optimization.

Our problem in (11) maximizes a linear objective over a convex set. In this work, we used Gurobi optimization toolbox [20] to solve (11). We observe from (11) that the dwell time constraints due to (2), (3), and (8) only depend on the LiDAR hardware. These constraints do not change with the location of the ego vehicle. The scene awareness constraint due to (10), however, changes with the ego vehicle's location and orientation. Therefore, (11) needs to be solved at each location of the ego vehicle. As our formulation depends only on the LiDAR hardware and the static scene topology maps, this problem can be solved offline for a predetermined navigation path. An optimized codebook of LiDAR settings can be generated for this path, allowing the ego vehicle to load the appropriate scan profile based on its location. The codebook-based approach reduces real-time computational complexity compared to the case where the ego vehicle solves (11) at each location.

We now summarize how the solution of (11), defined as $\{(r_i^\star, T_{\text{dwell},i}^\star)\}_1^N$, is realized with our custom hardware. To perceive sector i, the scanning range is set to $r_i^\star$ by configuring the LiDAR's ranging duration to $\delta_{\min}(r_i^\star)$. Furthermore, the instantaneous spin rate of the rotating platform is set to

$$\omega_i^\star = \frac{2\pi/N}{T_{\text{dwell},i}^\star} \tag{12}$$

when scanning sector i. ELLAS configures the ranging duration and the spin rate simultaneously for each sector. We provide details of our hardware setup to enable this simultaneous configuration in Section IV-A.

B. Interpretation of the Optimized Solution

We discuss the solution of (11) for the scene in Fig. 5(a), by considering $N = 8$ sectors and $\omega_{\max} = 4.32$ rad/s. The ego vehicle in this scene has access to $d_{\text{stat},i}$s in Fig. 6(b) from the static scene topology map. For frame rates of $F = 0.25$ fps and $F = 0.5$ fps, we find the optimized scanned ranges ($r_i^\star$s) and the optimized spin rates ($\omega_i^\star$s). We compare these profiles against those of a standard spinning LiDAR in Figs. 7 and 8. As a standard LiDAR does not leverage any scene awareness, its profile denoted by $(r_i^{\text{std}}, \omega_i^{\text{std}})$ remains the same over all

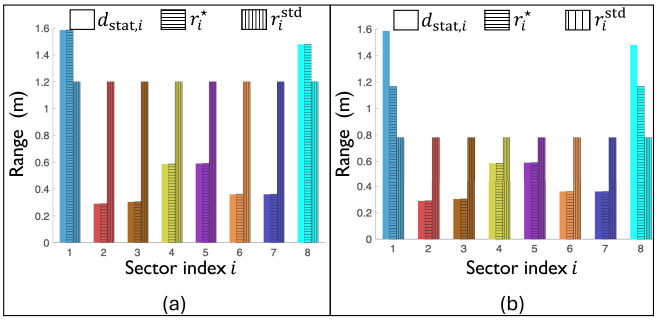

Fig. 7. For the scene in Fig. 5, the plots show the scanned range profiles with ELLAS and a standard LiDAR for 0.25 and 0.5 fps. Unlike a standard LiDAR that employs a uniform scan profile, ELLAS uses static scene topology maps to adapt the LiDAR's range over different sectors. (a) $F = 0.25$ fps. (b) $F = 0.5$ fps.

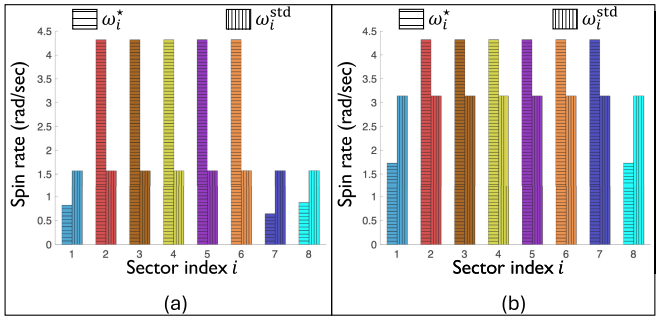

Fig. 8. For the scene in Fig. 5, the plots here show the instantaneous spin rate profiles with ELLAS and a standard LiDAR for frame rates of 0.25 and 0.5 fps. With the optimized profile in ELLAS, the LiDAR spins faster in sectors with closer static obstacles, for example, sectors 2–7, and vice versa. (a) $F = 0.25$ fps. (b) $F = 0.5$ fps.

i. To compute them, we first observe that a standard LiDAR spends an equal amount of time in any sector, that is, $T^{\text{std}}_{\text{dwell},i} = T/N = 1/(NF)$, which corresponds to an instantaneous spin rate $\omega_i^{\text{std}} = 2\pi F$ for any i. Next, we find the maximum range of this LiDAR by solving the feasibility constraint in (8) under equality, that is, $T^{\text{std}}_{\text{dwell},i} = \beta_2^\star (r_i^{\text{std}})^2 + \beta_1^\star r_i^{\text{std}} + \beta_0^\star$. We use $T^{\text{std}}_{\text{dwell},i} = 1/(NF)$ to write the quadratic equation

$$\beta_2^\star \left(r_i^{\text{std}}\right)^2 + \beta_1^\star r_i^{\text{std}} + \beta_0^\star = \frac{1}{NF}. \tag{13}$$

The largest positive root of (13) yields the maximum range of a standard LiDAR under the same constraints as in ELLAS. In our setup, this evaluates to $r_i^{\text{std}} = 1.2$ m at $F = 0.25$ fps and $r_i^{\text{std}} = 0.78$ m at $F = 0.5$ fps.

We now examine the scanning profiles in Figs. 7 and 8 for frame rates of 0.25 and 0.5 fps. On the one hand, ELLAS meets the scene awareness constraint in (10) and achieves a scanned range profile ($r_i^\star$s) that aligns well with the distance to known static obstacles ($d_{\text{stat},i}$s). On the other hand, a standard LiDAR results in a uniform range profile over the sectors which is inefficient. For instance, a standard LiDAR employs a longer range than what is needed for sectors 2–7. As these sectors have closer known static obstacles (see Fig. 5), ELLAS reduces the range of its LiDAR while scanning them. Furthermore, ELLAS achieves a longer range than a standard LiDAR in sectors 1 and 8, which focus on the main lane. We also observe from Fig. 7(a) and (b) that increasing the frame rate reduces the scanned range of a standard LiDAR. This is because of the shorter dwell time at a higher frame rate, for which the LiDAR cannot scan farther distances (see Fig. 4 for reference). Finally, we notice from Fig. 8 that ELLAS spins faster in sectors 2–7 with closer known static obstacles. This allows ELLAS to save time in a rotation, which is used to scan sectors 1 and 8 at a low spin rate. A low spin rate corresponds to a longer dwell time, which enables ELLAS to enhance the range and resolution in these sectors.

IV. Proof-of-Concept ELLAS System

We use the miniature driving setup in Fig. 5(a) to evaluate ELLAS using an experiment and simulations. The experiment is done at a frame rate of $F = 0.25$ fps, for a randomly chosen ego vehicle's location and a test target. To evaluate the statistical performance of the system, we consider simulations with an ensemble of ego vehicle locations within the digital map in Fig. 5(b).

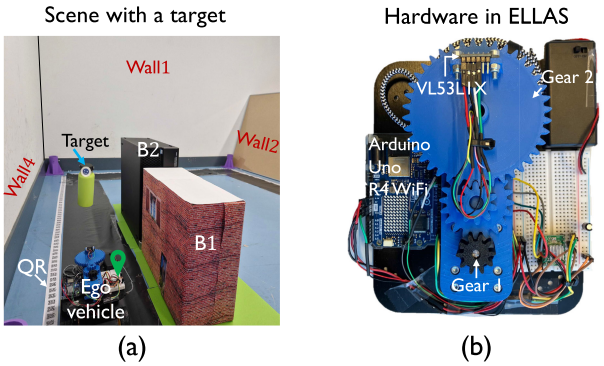

Fig. 9. In our experiment, a miniature pedestrian is introduced on the lane as a target in the scene. We study if ELLAS detects this target shown in (a). Our custom-made hardware in ELLAS, which achieves simultaneous range and resolution adaptation over different sectors, is shown in (b). This hardware is mounted on the ego vehicle as seen in (a).

A. Experiment

In our experiment, we study how ELLAS detects a miniature pedestrian shown in Fig. 9(a). The pedestrian is placed at (0.24, 1.65 m) and it is unknown to our system before the LiDAR scans the scene. Most importantly, the pedestrian is not part of the static scene topology map used by ELLAS. In this section, we discuss our procedure to estimate the ego vehicle's pose, solve (11) using the estimated pose and the static map in Fig. 5(b), and apply the optimized settings in our system for target detection.

1) Pose Estimation: We use a Bluetooth-enabled playstation controller to drive our ego vehicle, the robot, along the lane in Fig. 5(a). To identify the robot's location, we use a sequence of QR codes along the left side of the lane, each encoding a distinct position. These QR codes are linearly spaced at 3 cm, thereby providing a localization accuracy of 1.5 cm along the lane. The QR-based approach was previously introduced in [21] and [22] as a low-cost solution for indoor localization. In practice, ultrawideband (UWB) [23], [24] or Wi-Fi-based systems [25], [26] can be employed for indoor

positioning, while GPS or cellular networks can be used for outdoor localization [27], [28]. Additionally, inertial sensors on vehicles can be leveraged to estimate the orientation [29].

The robot is stopped at an arbitrary location on the path and its pose is estimated by scanning the QR code next to it. The QR code, captured by a downward-facing phone camera on the robot, is relayed to a local server using an IP Webcam application [30]. The local server, a laptop, decodes the scanned QR code using OpenCV [31] and then identifies the pose. In our experiment, the robot's location was identified as $(x_e, y_e) = (0.24, 0.45\text{ m})$ and its orientation is decoded as $\theta_e = 90°$ based on the path on which it is traveling.

2) LiDAR Parameter Optimization: To optimize the LiDAR parameters, ELLAS uses the predetermined static scene topology map in Fig. 5(b) and the real-time pose received from the robot. This information is used to first compute the distance to the closest static obstacles in each sector, that is, $d_{\text{stat},i}$s. These values are shown in Fig. 6(b) for $(x_e, y_e, \theta_e) = (0.24\text{ m}, 0.45\text{ m}, 90°)$ and the topology in Fig. 5(b). Then, the optimization problem in (11) is solved at the server for the desired frame rate. We use $N = 8$ sectors and $\omega_{\max} = 4.32$ rad/s for the rotor speed limit. The optimized spin rate and scanned range profiles over the N sectors are transferred back to the robot by Wi-Fi.

3) Implementation of Optimized LiDAR Parameters: The robot applies the optimized parameters to our custom-made hardware that allows both range and resolution control. Our hardware comprises an Arduino Uno R4 Wi-Fi board, a stepper motor and its driver, a spinning platform, and the VL53L1X LiDAR. The LiDAR is mounted on top of the spinning platform as shown in Fig. 9(b). The rotational power is transferred from the stepper motor that drives gear 1 to the platform mounted on gear 2. Here, we use a gear ratio of 1:8 between the two gears. This gear ratio ensures that the LiDAR system spins at low rotational speeds without vibrations.

The Arduino keeps track of the LiDAR's scanning direction, which is used to determine the sector i according to (1). In sector i, the Arduino configures the LiDAR's ranging duration, called the timing budget in [15], corresponding to $r_i^\star$ using Fig. 2. In our work, $r_i^\star$ is ceiled to the nearest multiple of 0.5 m and the ranging duration associated with the ceiled $r_i^\star$ is applied to the LiDAR. The ceiling operation allows our Arduino to directly use the datapoints acquired in Fig. 2, without requiring any sophisticated interpolation. In addition to controlling the LiDAR, the Arduino also sets the rotational speed of the spinning platform to $\omega_i^\star$. This is achieved by setting the speed of the stepper motor to $8\omega_i^\star$, accounting for a gear ratio of 8 in our setup. The LiDAR point cloud acquired with the optimized settings in ELLAS is stored on the Arduino. As a benchmark, the point cloud with a standard LiDAR is also acquired and stored on the Arduino. The standard LiDAR function is achieved by employing uniform settings, that is, the constant spin rate of $\omega_i^{\text{std}} = 2\pi F \forall i$ and a uniform ranging duration corresponding to the ceiled r_i^{std}. The ceiling operation is the same as the one used in ELLAS, to ensure a fair comparison.

4) Results: The point cloud acquired by our robot comprises polar coordinates of the form $(r^{(p)}, \theta^{(p)})$, where p is the index of the point cloud measurement. The measurement $(r^{(p)}, \theta^{(p)})$ indicates that there is a target at a range of $r^{(p)}$ from the robot along direction $\theta^{(p)}$. Transferring the point cloud data wirelessly to our server was challenging, due to limited SRAM on the Arduino. To address this problem, we perform 8-bit uniform quantization of the point cloud data, that is, $(r^{(p)}, \theta^{(p)})$s, by assuming a maximum range of 3.5 m and a maximum angle of 360°. As a result of this quantization, the range and angular resolutions of our system are, respectively, limited to 1.3 cm and 1.41°. The Arduino sends the quantized point cloud measurements to the server, for ELLAS as well as the standard LiDAR. Finally, the server displays these point clouds over the static scene topology map. The point cloud results from our experiment are shown in Fig. 10 for the scene in Fig. 9(a), which includes a target.

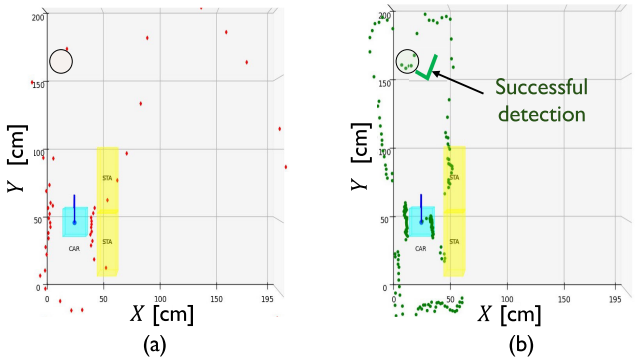

Fig. 10. LiDAR point clouds acquired with a standard LiDAR and ELLAS at a frame rate of 0.25 fps. ELLAS employs an optimized scanning profile which results in a high-density point cloud representation of the target. Here, the standard LiDAR fails to detect the target. (a) Standard. (b) ELLAS.

Fig. 10(a) and (b) shows that ELLAS acquires multiple point cloud measurements of the pedestrian located on the main lane, whereas the standard LiDAR does not. This is expected, as ELLAS achieves a longer scanned range along the main lane (sectors 1 and 8) compared to the standard LiDAR. Furthermore, the angular resolution with ELLAS is higher in sectors 1 and 8 as the spin rate is lower. Thus, ELLAS acquires a high-density point cloud representation of the target by enhancing the LiDAR's range and resolution in critical sectors. Such high-density point cloud representations are key to the high performance of object detection algorithms.

B. Simulation Results

We benchmark ELLAS against a standard LiDAR by considering an ensemble of ego vehicle locations in the static scene topology in Fig. 5(b). We adopt a simulation-based approach as obtaining real-time point clouds with our experiment can take significant time. This is due to the time needed to drive the robot, solve (11), and communicate with the server.

In our simulations, the robot is placed at all coordinates on a 2×2 m rectangular grid, except for those in the buildings B1 and B2. The rectangular grid has a resolution of 1×1 cm. Without loss of generality, we assume that the robot is oriented along the y-axis at any location. For each of the ~40 000 locations on the rectangular grid, the distance to

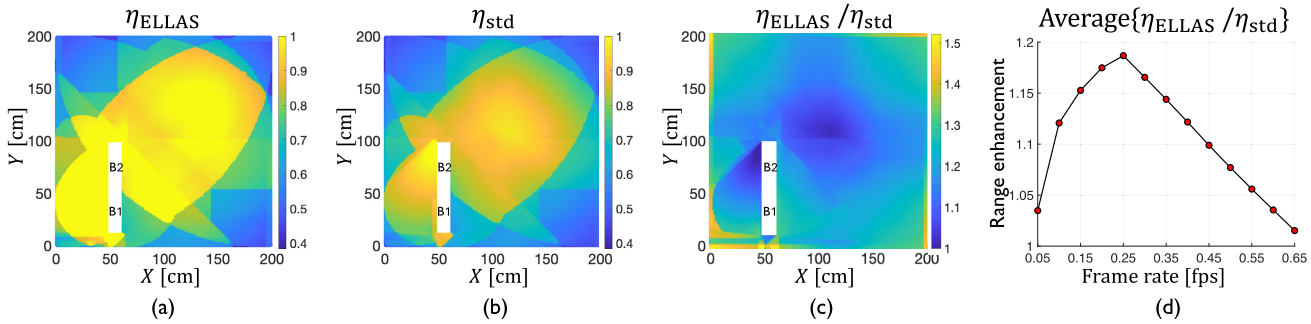

Fig. 11. We consider a frame rate of $F = 0.25$ fps in (a)–(c). The heatmaps in (a) and (b) show the fraction of drivable range scanned with ELLAS and a standard LiDAR at different ego vehicle locations. Enhancement in the drivable range scanned with ELLAS, that is, $\eta_{\text{ELLAS}}/\eta_{\text{std}}$ is shown in (c). We observe that this enhancement is large when the ego vehicle drives close to the boundary. Average enhancement with the frame rate is shown in (d).

static obstacles, that is, $d_{\text{stat},i}$s, is computed for $N = 8$ sectors using the digital map in Fig. 5(b). Our simulations use the same settings as our experiment, that is, $\omega_{\max} = 4.32$ rad/s and (8). Finally, (11) is solved for 14 different frame rates, at each location of the robot. The frame rates are varied from 0.05 to 0.65 fps in steps of 0.05 fps.

We evaluate ELLAS in terms of the fraction of drivable space that is reliably scanned by the LiDAR, denoted by η. This metric was proposed in [17] for scene-aware automotive radars and is defined as follows:

$$\eta = \frac{\sum_{i=1}^{N} \min(r_i, d_{\text{stat},i})}{\sum_{i=1}^{N} d_{\text{stat},i}} \tag{14}$$

where $0 \leq \eta \leq 1$. A higher η ensures that the LiDAR scans a larger fraction of the drivable space, which is desirable in automotive driving and navigation applications. This is because sensing solutions with a higher η allow early detection of targets than those with a lower η.

We show the fraction of the drivable range scanned with ELLAS and a standard LiDAR in Fig. 11(a) and (b), respectively. These fractions, denoted by η_{ELLAS} and η_{std}, are computed for the same frame rate of 0.25 fps. We observe from (14) that η does not improve if the LiDAR employs a scanned range that exceeds $d_{\text{stat},i}$ in sector i. While a standard LiDAR's scanned range may exceed this bound in some sectors, ELLAS never exceeds the bound as it optimizes under the scene awareness constraint in (10). By limiting the range in sectors with closer static obstacles, ELLAS saves on the dwell time to enhance scanned range in sectors with farther static obstacles. Therefore, we expect the scanned fraction with ELLAS to be at least that of a standard LiDAR, that is, $\eta_{\text{ELLAS}} \geq \eta_{\text{std}}$. This observation that $\eta_{\text{ELLAS}}/\eta_{\text{std}} \geq 1$ can also be made from Fig. 11(c) which shows the ratio over all locations.

Fig. 11(c) indicates that $\eta_{\text{ELLAS}}/\eta_{\text{std}}$ varies spatially over the rectangular grid. This is because $d_{\text{stat},i}$s as well as the optimized configuration in ELLAS vary with the ego vehicle's location. Finally, we observe from Fig. 11(c) that the enhancement in scanned range with ELLAS, that is, $\eta_{\text{ELLAS}}/\eta_{\text{std}}$, is large when the ego vehicle is close to the wall boundaries. This is because $d_{\text{stat},i}$s are small in sectors facing the walls, which allows ELLAS to significantly extend its scanned range in other sectors. Finally, we study the average $\eta_{\text{ELLAS}}/\eta_{\text{std}}$ with the frame rate using Fig. 11(d). For each frame rate, the average is taken over all possible locations of the ego vehicle. Fig. 11(d) shows that the standard LiDAR achieves similar performance as ELLAS at low or high frame rates. At low frame rates, the dwell time with a standard LiDAR, that is, $1/NF$, is sufficient to scan up to its maximum range (3.5 m) in all sectors. At high frame rates, however, the LiDAR has limited dwell time and its scanned range is shorter than $d_{\text{stat},i}$s. In both cases, the scene-aware constraint in (10) does not determine the solution of (11) and $\eta_{\text{ELLAS}}/\eta_{\text{std}}$ approaches 1.

V. Scaling up ELLAS to Automotive Driving: Challenges and Potential Solutions

ELLAS assumes that the ego vehicle's pose is perfectly known, to determine the optimal LiDAR configuration under scene awareness. In an automotive application, however, GPS inaccuracies and orientation estimation errors can lead to ELLAS optimizing the LiDAR configuration for a mismatched pose. This mismatch may result in the ego vehicle employing suboptimal LiDAR parameters for its pose. To address this issue, one approach is to model localization uncertainty and extend our formulation in (11) using a stochastic optimization (SO) approach. For automotive radars, it was shown in [17] that SO-based beamformers were still able to leverage scene awareness while being robust to practical localization errors.

In our implementation, the optimization problem was solved at a local server, as the Arduino on the robot has limited memory and processing power compared to the server. As a result, our setup currently requires about a minute to acquire a point cloud due to communication latency with the server. To meet real-time application requirements, navigation applications could precompute optimal LiDAR settings as a function of location. These settings can be calculated in advance using ELLAS, by leveraging LiDAR characteristics and offline street maps. A codebook of the optimized configurations can then be constructed, allowing the LiDAR system to load the optimized configuration on the fly with minimal on-board computing. While ELLAS facilitates the design of location-based codebooks, deriving a codebook of optimized configurations is challenging with the methods in [11], [12], and [13]. This is because the techniques in [11], [12], and [13] require real-time computation of the region of interest for LiDAR scan optimization.

TABLE I
COMPARISON OF ELLAS AND VELODYNE VLP-16 SPECIFICATIONS.

Specification	Our system in ELLAS	Velodyne VLP-16 [8]
Angular resolution	1.41°	0.1°-0.4°
Maximum range	4 m	100 m
Vertical channels	1	16
Frame rate	<0.65 fps	5 - 20 fps

Our prototype is a proof-of-concept to demonstrate location-aware scan adaptation at a low-cost. Realizing ELLAS with an industry-grade automotive LiDAR is an interesting direction.

While our current system is suitable for certain indoor applications, scaling it for automotive use would require significant upgrades to the laser and rotor. This includes increasing the number of vertical scanning channels from 1 in our 2-D LiDAR to a higher number to enable 3-D scanning. Table I summarizes the specification differences between our prototype and a commercial LiDAR like Velodyne's VLP-16 sensor [8].

Although our paper focused on developing a proof-of-concept prototype, ELLAS can also be implemented on industry-grade spinning LiDARs through sector-specific programming of existing hardware. The scanned range can be adjusted across sectors by modifying the laser's ranging duration or intensity. Similarly, resolution adaptation can be achieved by varying the spin rate with the sector. For example, Velodyne's VLP-16 LiDAR allows spin rates between 300 and 1200 r/min. While the spin rate is typically fixed over an entire rotation, ELLAS proposes varying the rate by sector within the specified limits. Our formulation in (11) assumes that the spin rate can be abruptly changed at sector boundaries, ignoring the angular acceleration limits of the rotor. Optimizing continuous spin profiles that adhere to acceleration limits is beyond the scope of this article. Incorporating these additional constraints of an industry-grade automotive LiDAR into (11) would allow ELLAS to significantly enhance road safety with situation-aware scanning.

VI. CONCLUSION

In this article, we showed how spinning LiDARs can leverage static scene topology maps to adaptively scan the environment. To this end, we developed an end-to-end system called ELLAS that jointly optimizes the LiDAR's range and resolution over different sectors in its field of view. ELLAS reduces the scanned range of the LiDAR in sectors with closer known static obstacles and vice versa. Furthermore, ELLAS enhances the angular resolution of the LiDAR in sectors where static obstacles are far away. We constructed a miniature proof-of-concept driving setup and showed that ELLAS can successfully detect a pedestrian in the setup, while detection with a standard LiDAR fails. We also showed by simulations that ELLAS scans a larger fraction of the drivable region than a standard LiDAR.

ACKNOWLEDGMENT

The authors would like to thank Ralph Willekes for providing technical support in programming the Arduino.

REFERENCES

[1] Q. Zou, Q. Sun, L. Chen, B. Nie, and Q. Li, "A comparative analysis of LiDAR SLAM-based indoor navigation for autonomous vehicles," *IEEE Trans. Intell. Transp. Syst.*, vol. 23, no. 7, pp. 6907–6921, Jul. 2022.

[2] R. Border, N. Chebrolu, Y. Tao, J. D. Gammell, and M. Fallon, "Osprey: Multisession autonomous aerial mapping with LiDAR-based SLAM and next best view planning," *IEEE Trans. Field Robot.*, vol. 1, pp. 113–130, 2024.

[3] Y. Li and J. Ibanez-Guzman, "LiDAR for autonomous driving: The principles, challenges, and trends for automotive LiDAR and perception systems," *IEEE Signal Process. Mag.*, vol. 37, no. 4, pp. 50–61, Jul. 2020.

[4] I. Bilik, "Comparative analysis of radar and LiDAR technologies for automotive applications," *IEEE Intell. Transp. Syst. Mag.*, vol. 15, no. 1, pp. 244–269, Jan. 2023.

[5] A. Pandharipande et al., "Sensing and machine learning for automotive perception: A review," *IEEE Sensors J.*, vol. 23, no. 11, pp. 11097–11115, Jun. 2023.

[6] W. Xu, Y. Cai, D. He, J. Lin, and F. Zhang, "FAST—LIO2: Fast direct LiDAR-inertial odometry," *IEEE Trans. Robot.*, vol. 38, no. 4, pp. 2053–2073, Aug. 2022.

[7] Z. Liu, F. Zhang, and X. Hong, "Low-cost retina-like robotic LiDARs based on incommensurable scanning," *IEEE/ASME Trans. Mechatronics*, vol. 27, no. 1, pp. 58–68, Feb. 2022.

[8] Mapix. (2018). *Velodyne LiDAR Puck*. Accessed: Jan. 14, 2025. [Online]. Available: https://www.mapix.com/wp-content/uploads/2018/07/63-9229_Rev-H_Puck-_Datasheet_Web-1.pdf

[9] A. Elfes, "Using occupancy grids for mobile robot perception and navigation," *Computer*, vol. 22, no. 6, pp. 46–57, Jun. 1989.

[10] A. Geiger, M. Lauer, C. Wojek, C. Stiller, and R. Urtasun, "3D traffic scene understanding from movable platforms," *IEEE Trans. Pattern Anal. Mach. Intell.*, vol. 36, no. 5, pp. 1012–1025, May 2014.

[11] F. Pittaluga, Z. Tasneem, J. Folden, B. Tilmon, A. Chakrabarti, and S. J. Koppal, "Towards a MEMS-based adaptive LiDAR," in *Proc. IEEE Int. Conf. 3D Vis. (3DV)*, Nov. 2020, pp. 1216–1226.

[12] E. Gofer, S. Praisler, and G. Gilboa, "Adaptive LiDAR sampling and depth completion using ensemble variance," *IEEE Trans. Image Process.*, vol. 30, pp. 8900–8912, 2021.

[13] M. A. A. Belmekki, R. Tobin, G. S. Buller, S. McLaughlin, and A. Halimi, "Fast task-based adaptive sampling for 3D single-photon multispectral LiDAR data," *IEEE Trans. Comput. Imag.*, vol. 8, pp. 174–187, 2022.

[14] B. Tilmon et al., "Energy-efficient adaptive 3D sensing," in *Proc. IEEE/CVF Conf. Comput. Vis. Pattern Recognit.*, Jun. 2023, pp. 5054–5063.

[15] ST Microelectron. *VL53L1X Time-of-flight Sensor*. Accessed: Jan. 14, 2025. [Online]. Available: https://www.st.com/en/imaging-and-photonics-solutions/vl53l1x.html

[16] E. Focante, N. J. Myers, G. Joseph, and A. Pandharipande, "Situation-aware adaptive transmit beamforming for automotive radars," in *Proc. ICASSP - IEEE Int. Conf. Acoust., Speech Signal Process. (ICASSP)*, Apr. 2024, pp. 8621–8625.

[17] E. Focante, N. J. Myers, G. Joseph, and A. Pandharipande, "Adaptive beamforming for situation-aware automotive radars under uncertain side information," *IEEE Trans. Radar Syst.*, vol. 2, pp. 699–711, 2024.

[18] E. Focante, N. J. Myers, G. Joseph, and A. Pandharipande, "Transmit beamforming for phased array radars under uncertain occupancy grid map information," in *Proc. IEEE Sensors*, Oct. 2024, pp. 1–4.

[19] W. Wei, *ToF LiDAR for Autonomous Driving*. Bristol, U.K.: IOP Publishing, 2023.

[20] Gurobi Optim., LLC. (2020). *Gurobi Optimizer Reference Manual*. [Online]. Available: http://www.gurobi.com

[21] H. Zhang, C. Zhang, W. Yang, and C.-Y. Chen, "Localization and navigation using QR code for mobile robot in indoor environment," in *Proc. IEEE Int. Conf. Robot. Biomimetics (ROBIO)*, Dec. 2015, pp. 2501–2506.

[22] T. Liu, J. Kuang, W. Ge, P. Zhang, and X. Niu, "A simple positioning system for large-scale indoor patrol inspection using foot-mounted INS, QR code control points, and smartphone," *IEEE Sensors J.*, vol. 21, no. 4, pp. 4938–4948, Feb. 2021.

[23] C. Wang, A. Xu, J. Kuang, X. Sui, Y. Hao, and X. Niu, "A high-accuracy indoor localization system and applications based on tightly coupled UWB/INS/Floor map integration," *IEEE Sensors J.*, vol. 21, no. 16, pp. 18166–18177, Aug. 2021.

[24] B. Yang, J. Li, Z. Shao, and H. Zhang, "Robust UWB indoor localization for NLOS scenes via learning spatial–temporal features," *IEEE Sensors J.*, vol. 22, no. 8, pp. 7990–8000, Apr. 2022.
[25] Y. Wu, R. Chen, W. Li, Y. Yu, H. Zhou, and K. Yan, "Indoor positioning based on walking-surveyed Wi-Fi fingerprint and corner reference trajectory-geomagnetic database," *IEEE Sensors J.*, vol. 21, no. 17, pp. 18964–18977, Sep. 2021.
[26] M. Kotaru, K. Joshi, D. Bharadia, and S. Katti, "SpotFi: Decimeter level localization using WiFi," in *Proc. ACM Conf. Special Interest Group Data Commun.*, Aug. 2015, pp. 269–282.
[27] N. González-Prelcic et al., "The integrated sensing and communication revolution for 6G: Vision, techniques, and applications," *Proc. IEEE*, vol. 112, no. 7, pp. 676–723, Jul. 2024.
[28] F. Wen, H. Wymeersch, B. Peng, W. P. Tay, H. C. So, and D. Yang, "A survey on 5G massive MIMO localization," *Digit. Signal Process.*, vol. 94, pp. 21–28, Nov. 2019.
[29] J.-C. Juang and C.-F. Lin, "A sensor fusion scheme for the estimation of vehicular speed and heading angle," *IEEE Trans. Veh. Technol.*, vol. 64, no. 7, pp. 2773–2782, Jul. 2015.
[30] Thyoni Tech. *IP Webcam Application*. Accessed: Jan. 14, 2025. [Online]. Available: https://ip-webcam.appspot.com/
[31] G. Bradski and A. Kaehler, "OpenCV," *Dr. Dobb's J. Softw. Tools*, vol. 3, no. 2, pp. 120+122–125, Nov. 2000.

Thymon Rhemrev received the B.Sc. degree in mechanical engineering from Delft University of Technology, Delft, The Netherlands, in 2023. In his B.Sc. thesis project, he worked with his team to build ELLAS, the adaptive LiDAR in this article.

Mr. Rhemrev presented a live demonstration of ELLAS at IEEE SENSORS 2024 in Kobe, Japan, and gained recognition as a finalist for the Best Live Demo Award.

Emma de Jong received the B.Sc. degree in mechanical engineering from Delft University of Technology, Delft, The Netherlands, in 2024, with a minor in psychology from Leiden University, Leiden, The Netherlands.

Before her B.Sc., she spent a semester at the Instituto Lorenzo de Medici, Florence, Italy, and a summer at the Imperial College Business School, London, U.K., where she focused on business strategy and consulting. She is currently exploring the field of finance as an intern at a private equity firm.

Ms. Jong received the Best Live Demo Award finalist at IEEE Sensors 2024 for the work done during her B.Sc. thesis.

Gideon van Triest received the B.Sc. degree in mechanical engineering with a minor in computer science from Delft University of Technology (TU Delft), Delft, The Netherlands, in 2024. He is currently pursuing the Plant-Based Diploma with Le Cordon Bleu, Paris, France.

He is an ERP Developer with Metaltop BV, Vlaardingen, The Netherlands.

Mr. Triest received the Best Live Demo Award finalist at IEEE SENSORS 2024 for the work done during his B.Sc. thesis.

Roger Kalkman received the B.Sc. degree in mechanical engineering from Delft University of Technology (TU Delft), Delft, The Netherlands, in 2024, with a minor in international entrepreneurship and development from the Universidad de las Américas, Quito, Ecuador. He is currently pursuing the M.S. degree in sustainable energy technology with TU Delft.

Mr. Kalkman received the Best Live Demo Award finalist at IEEE SENSORS 2024 for the work done during his B.Sc. thesis.

Jordy Pronk is currently pursuing the B.Sc. degree in mechanical engineering with Delft University of Technology (TU Delft), Delft, The Netherlands.

Mr. Pronk received the Best Live Demo Award finalist at IEEE SENSORS 2024 for the work done during his B.Sc. thesis.

Ashish Pandharipande (Senior Member, IEEE) received the M.S. degree in electrical and computer engineering, the M.S. degree in mathematics, and the Ph.D. degree in electrical and computer engineering from the University of Iowa, Iowa City, IA, USA, in 2000, 2001, and 2002, respectively.

Subsequently, he was a Postdoctoral Researcher at the University of Florida, Gainesville, FL, USA; a Senior Researcher at the Samsung Advanced Institute of Technology, Suwon, South Korea; a Senior Scientist at Philips Research, Eindhoven, The Netherlands; and the Lead Research and Development Engineer at Signify, Eindhoven. He has held visiting positions at AT&T Laboratories, Florham Park, NJ, USA, and the Department of Electrical Communication Engineering, Indian Institute of Science at Bengaluru, Bengaluru, India. He is currently the Innovation Director of NXP Semiconductors, Eindhoven, The Netherlands. His research interests are in sensing, networking and controls, data analytics, and their applications in domains like autonomous mobility, smart lighting systems, and cognitive wireless systems. He has around 200 international conferences and journal publications and more than 100 patent grants/applications in these fields.

Dr. Pandharipande is a Senior Editor of IEEE SIGNAL PROCESSING LETTERS, a Topical Area Editor of IEEE SENSORS JOURNAL, and an Associate Editor of IEEE JOURNAL OF BIOMEDICAL AND HEALTH INFORMATICS.

Nitin Jonathan Myers (Member, IEEE) received the B.Tech. and M.Tech. degrees in electrical engineering from Indian Institute of Technology (IIT) at Madras, Chennai, India, in 2016, and the Ph.D. degree in electrical and computer engineering (ECE) from The University of Texas at Austin (UT Austin), Austin, TX, USA, in 2020.

He is currently a tenured Assistant Professor at Delft Center for Systems and Control, Delft University of Technology (TU Delft), Delft, The Netherlands.

Dr. Myers received the DAAD WISE Scholarship in 2014 and a Silver Medal, Institute Merit Prize, in 2016 while at IIT Madras. At UT Austin, he received the University Graduate Continuing Fellowship from 2019 to 2020 and the 2018 and 2019 ECE Research Awards from the Cockrell School of Engineering. His research won the IEEE ICASSP 2020 Video Contest Runner-Up, the Best Student Paper Award at IEEE SPAWC 2022, and the Best Live Demo Finalist at IEEE SENSORS 2024. In 2022, he was recognized as the Best Lecturer in the second year of the bachelor's program in mechanical engineering at TU Delft.